Manuscript
Click here to access/download;Manuscript;RevisedManuscript_3rd_Revision.
Accepted manuscript. Published in Journal of Geotechnical and Geoenvironmental Engineering (2021). Version of record: https://doi.org/10.1061/(ASCE)GT.1943-5606.0002667. This material may be downloaded for personal use only. Any other use requires prior permission of the American Society of Civil Engineers. This material may be found at https://doi.org/10.1061/(ASCE)GT.1943-5606.0002667.

Effect of grain crushing on the hydraulic conductivity of tailings sand

Shubjot Singh[1], Zygi Zurakowski[2], Sheng Dai[3], and Yida Zhang[4*]

ABSTRACT

Tailing dams are constructed to impound the byproducts of mining operations and are often built using the coarser fraction of the tailings resulting from gravity separation processes. The high stresses anticipated at the bottom of tall tailings dams can lead to grain crushing resulting in a reduction in the hydraulic conductivity, and ultimately long-term performance issues if the water drains at a slower rate than required. Therefore, in order to accurately evaluate the margin of safety in designing tall tailings dams, understanding the evolution of the hydro-mechanical behavior of the tailings is important. This paper presents the results from a series of laboratory-scale high-stress compression tests combined with hydraulic conductivity measurements using a specially designed oedometer cell. The experimental results were subsequently interpreted by an enhanced continuum breakage mechanics model. The grain-size distributions predicted by the continuum breakage model were further combined with six commonly used hydraulic models to predict the reduction of hydraulic conductivity of tailings sand subjected to grain crushing. The results suggest that a stress increase from 5 MPa to 40 MPa can cause an increase in fines content from 11% to 17% respectively, and corresponding reduction in hydraulic conductivity of up to one order of magnitude for the tested materials. The paper highlights that breakage mechanics theory combined

[1] Graduate student, University of Colorado-Boulder, Boulder, CO, USA
[2] Lead Geotechnical Engineer, Stantec, Denver, CO, USA
[3] Assistant Professor, Georgia Institute of Technology, Atlanta, GA, USA
[4] Assistant Professor, University of Colorado-Boulder, Boulder, CO, USA. Corresponding author. Email: yida.zhang@colorado.edu

with proper hydraulic conductivity models can offer reliable predictions of the evolution of the hydromechanical behavior of tailings sands subjected to high stresses.

Keywords: breakage mechanics, grain breakage, high-stress compression, hydraulic conductivity, underflow tailings

INTRODUCTION

With the rapid growth of mining activities worldwide (Bebbington et al. 2008; Rogich and Matos 2008), the demand for tailings waste storage is increasing significantly. One of the most common storage methods is to construct a tailings storage facility (TSF), whereby the tailings are deposited in isolated impoundments behind the so-called tailings dams. These dams typically are constructed starting with a relatively small dam, referred to as a starter dam, that gradually grows in height as the storage demand increases over the operational life of the facility. Currently, there are more than 3500 tailings dams worldwide (Burritt and Christ 2018; Davies et al. 2000) which contain billions of tons of waste material from mineral processing. The consequences associated with a tailing dam failure can be devastating. For example, the most recent Brumadinho dam disaster, which occurred in January 2019 in Brazil, caused more than 250 fatalities, over $2.88 billion in property damage and release of around 12 million cubic meters of tailings waste to the environment (Thompson et al. 2020). Fearing such catastrophic consequences, the short- and long-term stability of tailings storage facilities (TSFs) becomes a critical consideration in their design, construction, and operation.

One of the factors that can contribute to the risk of instability of a TSF is the evolution of the engineering properties of the materials comprising the dam over time. The materials used in constructing tailings dams usually come from local quarries or the mining process. For the latter,

a hydro-cycloning process commonly is used to separate the raw tailings produced by milling into coarse and fine fractions which are referred to as the underflow and the overflow materials, respectively. The underflow material is used to construct and raise the height of the dam due to its relatively high hydraulic conductivity and strength and low compressibility, whereas the overflow material is deposited in slurry form at the upstream side of the dam. Due to the high hydraulic head in the upstream, as well as the application of construction water from underflow slurry deposition, maintaining good drainage conditions inside the dam is critical to avoid saturation of the underflow material, thereby minimizing liquefaction potential. As a result, strict quality control is often imposed on the cycloning process, e.g., the underflow is required to have less than about 15% - 18% of fines (Barrera et al. 2011; Valenzuela 2018). However, even if such a requirement is satisfied at the time of construction, the gradation of the underflow can evolve over time due to sustained mechanical and environmental (e.g. hydraulic, chemical and thermal) loadings. As the height of the TSF increases, the stresses at the base can exceed several mega pascals which may be sufficient to initiate grain crushing. This grain crushing can effectively increase the fines content, leading to pore clogging and reduced hydraulic conductivity, and eventually jeopardize the stability of the dam.

For these reasons, there is a pressing need to better understand the hydromechanical behavior of tailings underflow in the context of grain crushing. Only a few experimental studies have been reported in this regard. Riemer et al. (2008) conducted monotonic and cyclic triaxial compression tests on an underflow material from the Cerro Verde Mine in southern Peru and showed that the fines content increased by 5~6% when consolidated from 0 to 5.5 MPa. Promoted by grain crushing, the tailings sand appeared to be substantially more contractive and less cyclically resistant at high stress. Undrained triaxial compression tests were conducted by Fourie and

Papageorgiou (2001) to delineate the possible steady-state line for tailings with different fines content, demonstrating the possibility of static liquefaction in the case of Merriespruit tailings dams in South Africa. Bedin et al. (2012) showed the possibility of flow instability at low stress levels due to the pronounced contractive behavior exhibited by gold tailings at low stress levels. These studies, however, have extensively focused on the mechanical aspect. Little is known about the co-evolution of hydraulic conductivity with respect to grain crushing and porosity reduction for tailings underflow. Such information is important in estimating the phreatic level and moisture distribution in the TSF prior to any stability or deformation analysis.

The goal of this study is to: 1) quantify the effect of compaction and grain crushing on the hydraulic conductivity of tailings sand, and 2) establish and validate a predictive model that can simultaneously capture the evolution of porosity, gradation and hydraulic conductivity of granular soils subjected to high-stress loading. To achieve this goal, a series of high-stress oedometer tests coupled with simultaneous hydraulic conductivity measurements on tailings sand are performed using a customized oedometer cell. Then, the test results are interpreted using the Breakage Mechanics theory (Einav 2007) with an enhanced breakage evolution law. The predicted gradation and porosity are coupled with several hydraulic models to give hydraulic conductivities at different stress levels. Finally, the predicted hydraulic conductivity values are compared against the measured values and conclusions are drawn.

MATERIALS AND METHODS

Material and Properties

The soils being investigated in this study are underflow tailings and filter material from an active mine site. The underflow sand is the coarse fraction of tailings obtained from the cycloning process and is the main component of the tailings dam. The filter material is located at the interface

between the drainage system and the tailings sand at the bottom of the dam and is produced from crushed igneous intrusive rocks such as grandodiorite. The physical properties of the materials, including specific gravity, grain-size distribution (GSD), and maximum and minimum void ratios are summarized in Table 1. The GSDs are shown in Fig. 1a and the images of uncrushed underflow tailings and filter sand are shown in Fig. 1b and Fig. 1c, respectively. The underflow tailings has an overall smaller grain sizes with more angular shapes compared to the filter sand.

Equipment and Procedure

The test program included 10 oedometer tests, loaded to different maximum vertical stresses ranging from 3.5 MPa to 120 MPa, combined with in-test hydraulic conductivity measurements and post-test GSD analyses. Although stresses greater than 5 MPa, which is equivalent to 333 m-high overburden with dry unit weight of 15 kN/m^3 (Obermeyer and Alexieva 2011), are rare in tailings dams, loading to extended stress level allows for the examination of post-crushing compressibility which is useful for calibrating constitutive models. All oedometer tests were performed using a specially designed high-stress permeability (HSP) oedometer cell to accommodate elevated stresses of up to 160 MPa and permit the measurement of hydraulic conductivity without unloading the specimen. Fig. 2a shows the three-dimensional (3D) isometric view of the designed high-stress permeability (HSP) oedometer cell. A thin Teflon ring is installed at the soil-steel interface to reduce the side friction during the one-dimensional (1D) deformation of the specimen. Water flow through the specimen is enabled by a drainage line in the piston and the base of the cell. A cob-web structure and a metallic porous disc are included at the top and the bottom of the specimen to facilitate the distribution of the water pressure. Because conventional porous stones may be damaged at high stress levels, sintered metallic porous discs made of stainless steel are used instead. O-rings are utilized to make a seal around the piston and the base

to prevent water leakage during hydraulic conductivity testing. High strength Grade 416 stainless steel was used to manufacture the piston, confining ring and the base. The assembled oedometer is shown in Fig. 2b**.** Vertical loading is provided by a 500-kN Universal Testing machine (UTM) (MTS 318.50 manufactured by MTS Systems Corporation-based in Minnesota). The combined oedometric compression and hydraulic conductivity tests are performed at five vertical stress levels (3.5 MPa, 5 MPa, 10 MPa, 40 MPa and 120 MPa) for both underflow tailings and filter sand. After each test, the specimen was subjected to wet sieve analysis (ASTM D1140-17) to obtain the post-loading GSD curve.

The HSP cell, however, cannot supply the back pressure for saturation as in conventional triaxial tests. To overcome this limitation, specimens were carefully prepared using the wet pluviation method which is routinely assumed to produce saturated (Bardet 1997; Chaney and Mulilis 1978; Ghionna and Porcino 2006) specimens for granular soils. Before pouring the sand, the cell was filled with water and the base outlet was flushed and closed to ensure the drainage lines were free of entrapped air bubbles (ASTM D5856-15). Soils were gradually poured and compacted by gently tamping each layer in multiple layers of similar height to achieve uniform density. Both the underflow tailings and filter sand specimens were prepared to 80% relative density in the HSP cell. The nominal radius and height (H_s) of the prepared specimen was 28 mm and 25 mm, respectively. Following compaction, the top porous disc and piston were slowly inserted in the cell and made to rest on the sample. The top drainage line was kept open to allow water drainage during this process. The assembled oedometer cell was then carefully placed on the loading platform (Fig. 2c). De-aired water was passed through the entire setup to expel any trapped air bubbles. Prior to loading, the inlet was kept open with the outlet valve closed. Compression was conducted at a loading rate of 4.5 kN/min which was sufficiently slow to allow full drainage of the specimen. After reaching

the target stress level, the test was paused, and the inlet valve was connected to the manometer for measuring the hydraulic conductivity using the falling head method (Fig. 2c).

Calibration for the Hydraulic Conductivity Measurement

Early trials showed that the measured hydraulic conductivity of the tested samples from the HSP cell is lower than the expected values for both materials. This was attributed to the resistance to water flow contributed by the drainage lines and the porous metallic discs at the base and the top of the specimen (Fig. 3a). In other words, the HSP cell itself may have some intrinsic resistance to fluid flows, acting as an additional porous unit in series connection with the soil specimen (Fig. 3b). To establish a correlation chart between the true hydraulic conductivity of the soil k_s and the apparent hydraulic conductivity measured from the HSP cell, k_a, two series of permeability tests were conducted on reference soil specimens which are made of silica sand mixed with non-plastic fines. The first series uses the standard permeameter with the falling head method (ASTM D5856-15) to determine the k_s of several reference samples prepared with varying fines content to achieve a wide range of k_s values (on the order of $10^{-8} \sim 10^{-3}$ m/s). In the second series, the apparent hydraulic conductivities (k_a) of the previously tested specimens at the same void ratios were re-measured using the HSP cell without vertical loading. Considering the possible effect of HSP sample height H_s, the second series was repeated three times with H_s = 15 mm, 25 mm and 38 mm to establish a $k_a - k_s$ correlation at different sample heights. The test results are plotted in Fig. 4.

Two observations can be made from the test results in Fig. 4. First, the hydraulic conductivity measurement using the HSP cell is sensitive to the height of the specimen, especially at the lower hydraulic conductivity values. Second, there is an upper bound value of k_a (i.e. 10^{-8} m/s) that can be measured by the HSP cell, beyond which k_a becomes insensitive to the true conductivity of the soil. This behavior can be explained by the series model in Fig. 3b. If the soil has a much lower

hydraulic conductivity than the cell element, the apparent conductivity of the system is dominated by the soil, and, thus the correlation is more sensitive to the soil's true hydraulic conductivity and the height of the specimen prepared; Conversely, the hydraulic conductivity of the cell dominates when the soil is highly permeable and, thus, the apparent hydraulic conductivity becomes independent of k_s.

Using the 1D series model in Fig. 3b, the apparent hydraulic conductivity of this system can be expressed by:

$$k_a = \frac{H_c + H_s}{\frac{H_c}{k_c} + \frac{H_s}{k_s}} \tag{1}$$

or

$$\frac{1}{k_a} = \frac{H_c / (H_c + H_s)}{k_c} + \frac{H_s / (H_c + H_s)}{k_s} = \frac{1}{B} + \frac{A}{k_s} \tag{2}$$

where k_s and H_s are the hydraulic conductivity and height of the soil specimen, respectively; k_c and H_c are the equivalent hydraulic conductivity and height of the cell element, respectively (Fig. 3b); $A = H_s / (H_c + H_s)$ and $B = (H_c + H_s) k_c / H_c$ are two model parameters defined for conciseness. Eq. (2), however, is found to be inadequate in capturing the $k_a - k_s$ data regardless of the choice of A and B parameters. This is not surprising because Eq. (2) is derived under the assumption of one-dimensional flow. This assumption is valid for soil columns with high length-to-diameter ratio, which is why standard permeameters are designed to be tall cylinders. The HSP cell sample, however, has an opposite aspect ratio (56 mm diameter and 25 mm height) with the purpose to minimize the lateral friction during high-stress compression tests. This is the same rational for the short specimens adopted in standard consolidation/ oedometer tests. For this reason,

177 the specimen boundaries, although coupled with a cob-web structure (Fig. 2a), may not be
178 sufficient to efficiently distribute water pressure in a uniform manner throughout the 25 mm
179 thickness, thus making the flow pattern inside the cell no longer one-dimensional. The relatively
180 low permeability of the porous discs adds further complication to the analysis. To account for these
181 factors and to better fit the experimental data, Eq. (2) is modified as follows:

182 $$\frac{1}{k_a} = \frac{1}{B} + \frac{A}{k_s^{\,n}} \tag{3}$$

183 where n is an empirical correlation coefficient. Note that Eq. (3) does not have physical basis, but
184 is simply adopted as a fitting function to smoothly represent the correlation data. The best-fit lines
185 are plotted in Fig. 4 and the corresponding parameters are summarized in Table 2. Throughout this
186 study, the value of k_a and the instantaneous sample height H_s obtained from the apparatus
187 measurements are input into the correlation chart Fig. 4 to obtain the true hydraulic conductivity
188 k_s of the soil specimen.

189 ***Experimental Results***

190 Results of the combined compression and hydraulic conductivity tests and the GSDs of post-loaded
191 specimens for the underflow tailings and the filter sand are shown in Fig. 5. The compression
192 curves in Fig. 5a and Fig. 5c exhibit two distinct slopes at low- and high-stress levels. Such a
193 response is typical for granular soils undergoing grain crushing (Hendron Jr 1963; Nakata et al.
194 2001; Pestana and Whittle 1995). The transition point corresponds to the onset of massive grain
195 breakage and is often referred to as clastic yielding (McDowell et al. 1996). Theoretical and
196 experimental studies have shown that the clastic yield stress σ_{vc} is higher for soils with stronger
197 particles, smaller grains, and denser packing (McDowell 2002; Nakata et al. 2001; Zhang et al.
198 2016). Here, however, the yield stress for both soils is about the same at 5 MPa, despite the smaller

average grain size (d_{50} = 0.15 mm) of the underflow tailings relative to that (d_{50} = 0.85 mm) of the filter sand. Considering these tests are conducted at the same relative density, the comprising minerals for the underflow tailings can be inferred to be much weaker than that of the filter sand. Petrography examinations indeed confirmed that the underflow tailings grains comprise quartz (~50%), muscovite and plagioclase, whereas the filter grains comprise predominately quartz (>90%). Also, the yielding transition is slightly more gradual for the underflow tailings compared to the filter sand. This difference is because the filter sand grains are more rounded and relatively brittle (Fig. 1c). Once stressed beyond the breakage threshold, sudden fracturing and comminution occurs, which is manifested as a sharp transition at the yielding point. For the underflow tailings with more angular (Fig. 1b) and smaller grains, the failure may involve local plastic sliding and deformation at the grain-to-grain contacts which blurs the clastic yielding transition. These observations are consistent with those by Nakata et al. (2001) and Zhang et al. (2017).

From the GSD curves in Fig. 5b and Fig. 5d, grain crushing apparently has already occurred at a stress level as low as 3.5 MPa before the apparent yielding stress of 5 MPa for both soils. The shifting in the GSD is more significant for the filter sand (Fig. 5d) due to a larger average grain size relative to that for the underflow tailings (see Fig. 1 and Table 1). The maximum grain size d_M for both materials stays the same during loading because of the so-called cushioning effect referring to the protection of larger grains from breakage due to distributed supports from the neighboring smaller grains (Mair and Abe 2008; Tsoungui et al. 1999). Inspection of the hydraulic conductivity data shows that the reduction of hydraulic conductivity is quite small before clastic yielding for both soils. This portion of hydraulic conductivity is mainly attributed to soil compaction and, thus, the reduction in porosity. After yielding, the hydraulic conductivity decreases significantly, caused by the combined effects of porosity reduction and fines generation.

For example, from 5 MPa to 40 MPa, the void ratio of filter sand decreased from 0.48 to 0.3 and the fines content increased from 11% to 17%, respectively, resulting in a hydraulic conductivity reduction by one order of magnitude. The reduction in hydraulic conductivity decreases at high stress levels where the void ratio, *e*, reaches about 0.1~0.2.

Continuum Breakage Theory

As evidenced in Fig. 5, the hydromechanical behaviors of granular soils are strongly affected by the microscale process of grain crushing. Significant effort has been devoted to quantifying the degree of grain breakage and link this with the stress-strain behavior of granular soils (Colliat-Dangus et al. 1988; Daouadji and Hicher 2010; Hagerty et al. 1993; Hardin 1985; Pestana and Whittle 1995; Xiao et al. 2016; Yamamuro and Lade 1996). Among them, the Continuum Breakage Mechanics (CBM) theory (Einav 2007) shows promising predictive capability in modeling crushable granular soils. The CBM formulation reflects the particle-continuum duality of granular soils by combining thermodynamic principles with micromechanical arguments. The model tracks the evolution of grain-size distribution (GSD) by introducing a breakage internal variable B and associating B with the release of elastic strain energy caused by grain fractures. The breakage B is defined in such a way that the current probability GSD, $g(x)$ can be computed by a linear interpolation $g(x) = (1\text{-}B)g_0(x)+Bg_u(x)$ where $g_0(x)$ and $g_u(x)$ are respectively the initial uncrushed and the ultimately crushed fractal GSDs with the following expressions:

$$g_0(x)=\frac{(3-\beta)x^{2-\beta}}{d_M^{3-\beta}-d_m^{3-\beta}};g_u(x)=\frac{(3-\alpha)x^{2-\alpha}}{d_M^{3-\alpha}-d_m^{3-\alpha}} \tag{4}$$

where d_m and d_M are the minimum and maximum grain diameter, respectively; α and β determine the uniformity of the initial and ultimate GSDs, respectively. The breakage B maps to the current GSD of the specimen, thus offering a mean to track the evolution of microstructural and

hydromechanical properties of the granular assembly throughout the course of loading. Such link also opens a pathway to integrate fracture mechanics with the continuum modeling of crushable soils, revealing the profound connection between the fracture toughness of grain minerals and the clastic yielding stress (Zhang et al. 2016), and between the delayed crack propagation and the time-dependent deformation of crushable soils (Zhang and Buscarnera 2017). Studies also have been conducted to couple the hydraulic and mechanical behaviors of granular soils within the framework of CBM (Ashari et al. 2016; Gao et al. 2016; Nguyen and Einav 2009; Zhang and Buscarnera 2015). These theories have been successfully applied in geotechnical engineering practices such as the interpretation of end bearing capacity of driven piles in sand (Zhang et al. 2013) and the determination of the long-term settlement of rockfill dams (Zhou et al. 2019). One issue with the original CBM, however, is that it tends to overpredict the rate of grain crushing with respect to stress increase (Park 2018; Zhang et al. 2017), possibly due to the lack of descriptors for grain shape and thus not distinguishing breakage events due to brittle splitting versus ductile abrasion at contact asperities. In what follows, we first revisit the breakage evolution law in the original CBM model and then seek for modifications to improve the model's ability in capturing realistic breakage evolution data.

The original breakage evolution law for the case of isotropic compression proposed in (Einav 2007) is expressed as follows:

$$E_B = \frac{E_c}{(1-B)^2} \tag{5}$$

where $E_B = -\partial\Psi / \partial B$ is the energy release rate due to an incremental change of breakage B and is referred to as the breakage energy; Ψ is the Helmholtz free energy; E_c is the critical breakage energy that controls the onset of breakage. It is straightforward to see that Eq. (5), together with

266 the definition of E_B which is associated with mean stress p (for the case of isotropic compression),
267 dictates a unique B-p relation for all granular materials (Einav 2007) despite the onset of B can be
268 controlled by E_c. This unique p-B relation implies that the model predicts the same shape of
269 breakage evolution curve regardless of the GSD, packing and grain shape of the soil.

270 For practical purposes, greater flexibility in this law is needed to capture the breakage evolution
271 of a wide range of natural soils with different rates of breakage growth, especially in the case of
272 Park (2018) and here. To develop such generalization, the yield surface is rewritten in the
273 dissipative stress space and the true stress space, respectively, as:

274 $$\bar{y} = \left(\frac{\bar{E}_B}{\sqrt{E_B E_c^*} / \cos\omega} \right)^2 + \left(\frac{\bar{p}}{\left(p / \sin\omega \right) \sqrt{E_c^* / E_B}} \right)^2 + \left(\frac{\bar{q}}{Mp} \right)^2 - 1 = 0 \tag{6}$$

275 $$y = \frac{E_B}{E_c^*} + \left(\frac{q}{Mp} \right)^2 - 1 = 0 \tag{7}$$

276 where q is the deviatoric stress; the superposed bar is used to distinguish the dissipative stresses
277 from the true stresses; M is the critical stress ratio related to the internal friction angle ϕ of the
278 material, i.e. $M = 6\sin\phi / \left(3 - \sin\phi\right)$ for triaxial compression; ω is a coupling angle controlling the
279 relative weight of energy dissipation through grain crushing and frictional sliding; and E_c^* is the
280 current breakage threshold that is a function of B. For example, if one specifies

281 $$E_c^* = \frac{E_c}{\left(1 - B\right)^2} \tag{8}$$

282 , then by substituting Eq. (8) into Eqs. (6) and (7), the yield surfaces of the original breakage
283 mechanics theory in (Einav 2007) can be retrieved. It is possible to show that the expression of E_c^*

284 governs the way B evolves with respect to the stress state. For example, enforcing isotropic loading
285 condition (i.e. q=0), Eq. (7) reduces to $E_B = E_c^*$ which, combined with Eq. (8), gives exactly the
286 original breakage evolution given by Eq. (5). Essentially, the yield condition in the form of Eqs.
287 (7) and (8) effectively decouples the breakage evolution law and the yield surface in the
288 hyperplastic formulation of CBM, allowing for convenient customization of the rate at which B
289 grows. With this result, a simple extension of Eq. (8) is proposed for better control over the shape
290 of the breakage evolution curve as follows:

291 $$E_c^* = \frac{E_c}{(1-B)^s} \tag{9}$$

292 where s is a shape factor. An analytical p-B relation for isotropic compression can be derived by
293 assuming an isotropic linear elasticity model in which $E_B = \vartheta K \varepsilon_v^{e2} / 2$ (Einav 2007) and enforcing
294 $E_B = E_c^*$:

295 $$p = \frac{1-\vartheta B}{(1-B)^{s/2}} \sqrt{\frac{2KE_c}{\vartheta}} \tag{10}$$

296 where K is the bulk modulus; and $\vartheta = 1 - \int_{D_m}^{D_M} g_u(x)x^2 dx \Big/ \int_{D_m}^{D_M} g_o(x)x^2 dx$ is the grading index where
297 g_u and g_0 are defined in Eq. (4). Fig. 6 shows the effect of s and E_c on the predicted p-B curves
298 along with the experimental data from an isotropic compression test on quartz sand by Park (2018).
299 The shape factor s controls the rate at which breakage evolves and thus can be adjusted depending
300 on the particle shape and the GSD of the natural soil (Fig. 6a). The role of critical breakage energy
301 E_c remains the same in controlling the onset of breakage (Fig. 6b).

Substituting Eq. (9) into the dissipative yield surface (6) and enforcing the orthogonality rule in the form of $\bar{p}=p,\bar{q}=q,\bar{E}_B=E_B$, the inelastic flow rule can be derived as:

$$\begin{aligned} d\varepsilon_v^p &= \lambda\frac{\partial\bar{y}}{\partial\bar{p}} = \lambda\frac{2\sin^2\omega}{p}\frac{E_B}{E_c^*} \\ d\varepsilon_s^p &= \lambda\frac{\partial\bar{y}}{\partial\bar{q}} = \lambda\frac{2q}{M^2p^2} \\ dB &= \lambda\frac{\partial\bar{y}}{\partial\bar{E}_B} = \lambda\frac{2\cos^2\omega}{E_c^*} \end{aligned} \tag{11}$$

where λ is the non-negative plastic multiplier; $d\varepsilon_v^p$ and $d\varepsilon_s^p$ are the volumetric and deviatoric components of plastic strain increment, respectively. To better represent the elastic response of granular soils, a pressure-dependent elasticity model (Einav and Puzrin 2004) is adopted and is defined through potential as:

$$\psi\left(\varepsilon_v^e,\varepsilon_s^e\right)=\frac{p_r}{\bar{K}\left(2-m\right)}A^{\frac{2-m}{1-m}}+\frac{3}{2}p_r\bar{G}A^{\frac{m}{1-m}}\varepsilon_s^{e2} \tag{12}$$

where $A=\bar{K}(1-m)\varepsilon_v^e+1$; p_r is a reference pressure usually taken as 1 kPa; $m=0.5$ for typical granular material; $\bar{K}$ and $\bar{G}$ are non-dimensional elastic constants; ψ is the grainsize specific Helmholtz free energy potential which is related to Ψ via $\Psi=\left(1-\vartheta B\right)\psi$. Combining the yield surface Eq. (7), flow rules Eq. (11) and free energy potential Eq. (12), the expression of λ can be obtained as detailed in Appendix A. This model is numerically integrated and used to perform the simulations.

Hydraulic Conductivity Models for Granular Media

Many empirical or semi-empirical models have been developed in the hydrology and geotechnical engineering communities to determine the hydraulic conductivity of soils based on their

319 microstructural properties such as the porosity and GSD. The first widely used formulation was
320 proposed by Hazen (1911). Kozeny (1927) proposed another formulation and was later modified
321 by Carman (1956) to become the celebrated Kozeny-Carman (KC) equation. This model includes
322 consideration of both porosity and GSD in predicting hydraulic conductivity and is therefore
323 considered to be more accurate than Hazen's model (Carrier 2003). Several other models that link
324 porosity and gradation indices with hydraulic conductivity have also been proposed (Alyamani
325 and Şen 1993; Creager et al. 1945; Slichter 1902; Terzaghi and Peck 1964). Studies have been
326 conducted to compare the overall predictive capabilities among these models for different porous
327 media (Boadu 2000; Cabalar and Akbulut 2016; Cheng and Chen 2007; DeJong and Christoph
328 2009; Ishaku et al. 2011; Odong 2007). Based on these studies, six commonly used hydraulic
329 conductivity models were chosen to be combined with the enhanced CBM model to predict the
330 evolution of hydraulic conductivity of tailings sand during 1D loading. The selected hydraulic
331 conductivity models are written in the following general form (Milan and Andjelko 1992):

332 $$k = \frac{g}{\nu} C\varphi(n) d_e^2 \tag{13}$$

333 where k is the hydraulic conductivity; g is the gravitational acceleration; ν is the kinematic
334 viscosity; C is a dimensionless sorting coefficient; $\varphi(n)$ is a function of porosity; d_e is the effective
335 grain size diameter. The expressions of C, $\varphi(n)$ and d_e for different hydraulic conductivity models
336 are summarized in Table 3. The combination of an empirical hydraulic model in Table 3 with the
337 CBM model provides a complete framework for evaluating the full stress-strain-GSD-hydraulic
338 conductivity response of granular soils subjected to high-stress loading. Specifically, the CBM
339 model provides the evolution of porosity and GSD as functions of stress. The porosity feeds into
340 the porosity function $\varphi(n)$, and the predicted GSD curves provides the effective grain diameter d_e

and the coefficient of uniformity C_u, enabling the prediction of the k via Eq. (13). The performance of the proposed hydromechanical model is evaluated in the following section.

RESULTS AND DISCUSSIONS

The experimental results obtained from the oedometer tests are used to calibrate and validate the proposed approach for both the underflow tailings and the filter sands. First, the model parameters are calibrated based on the compression response and the GSD data for both materials, as shown in Table 4. The elastic parameters are determined by matching the slope of the compression curve before yielding. The value of α is taken as 2.6 for the ultimate GSD (Sammis et al. 1987); β is determined by matching the GSD for the uncrushed material; ϑ is computed by integrating g_0 and g_u based on the definitions; E_c is determined by matching the yielding point in the compression curve; s is calibrated by matching the breakage evolution; and ω is determined by matching the slope of the compression curve after yielding.

The modeled and the measured compression responses for the underflow tailings are compared in Fig. 7a. The compression data are almost exactly captured by the CBM. With the newly proposed breakage evolution law given by Eq. (9), the predicted breakage curve captures the experimentally obtained breakage values at individual stress levels (Fig. 7a). Here the breakage data are computed from GSDs using the Einav (2007) definition for consistency. For a better comparison, the predicted B values are mapped to GSD curves as shown in Fig. 7b**.** One can observe that the range of GSD evolution is reasonably captured by the model with slight deviations at each stress level. These deviations are due to the simple GSD expression given by Eq. (4) which can only qualitatively represent the initial GSD of the underflow tailings. Nevertheless, the GSD data at small grain diameter (i.e. < 0.1 mm) are still well captured by the predicted GSDs, which provide an extrapolation tool to obtain d_{10} and d_{20} for the subsequent hydraulic conductivity determination.

Comparison of the model versus measured data for the filter sand is shown in Fig. 7c,d. Again, excellent agreement is observed on the compression and breakage evolution curves. The agreement between the modelled GSDs and measured GSDs is better for the filter sand (Fig. 7d) than the underflow tailings (Fig. 7b), given that Eq. (4) better represents the initial GSD of the filter sand.

The computed GSD curves and porosity are used to predict the hydraulic conductivity at each stress for both materials. The results are compared with experimental data in Fig. 8. Note that all mechanical parameters are fixed once calibrated in Fig. 7, such that there are no tunable parameters in the hydraulic conductivity models. Therefore, the results in Fig. 8 are true predictions rather than calibrations or best fits. For the underflow tailings (Fig. 8a), the Kozeny-Carman, Terzaghi and Breyer models provide the closest agreement with the experimental results for the lower and medium stresses (< 40 MPa). However, at the high-stress range (40 ~ 100 MPa), predictions from the Kozeny-Carman and Terzaghi models start deviating from the experimental results, whereas the Breyer model remains approximately accurate. The Terzaghi and Slitcher models underpredict the hydraulic conductivity regardless of the stress, which is consistent with the conclusions by Cheng and Chen (2007) and Odong (2007). The Hazen and the USBR models are inapplicable for the case where the coefficient of uniformity is greater than 5 ($C_u > 5$). Nonetheless, the predictions based on these models are compiled in Fig. 8a because the value of C_u is close to 5 for stresses below 40 MPa. Hazen's model underpredicts the hydraulic conductivity by almost two orders of magnitude at all stresses. In contrast, the USBR method slightly overpredicts the measured values but otherwise follows the overall trend well. For the filter sand (Fig. 8b), the Terzaghi, Breyer and Kozeny-Carman predicted values again match well with the experimental results at low stresses (< 40 MPa), whereas only the Breyer model follows the trend at high stresses (40 ~ 100 MPa). The primary difference with the underflow tailings is that the USBR model significantly overpredicts

387 the hydraulic conductivity for the filter sand, which may be attributed to the relatively high value
388 of C_u (7~ 25) even at low stresses. Based on these observations, Kozeny-Carman, Terzaghi and
389 Breyer model predict reasonably well the hydraulic conductivity of underflow tailings at stress
390 levels of up to 40-50 MPa, and the Breyer model is recommended for stresses higher than 50 MPa.
391 In practical applications for tailings dams where the maximum vertical stress is lower than 6~7
392 MPa, the Kozeny-Carman model offers the most accurate prediction compared to other models
393 used in this study.

394 **CONCLUSIONS**

395 This study presents the results of a series of coupled high-stress oedometric compression and
396 laboratory-scale hydraulic conductivity tests on tailings sands. A novel oedometer cell (HSP) is
397 designed and manufactured for this purpose. Two granular soils, namely a underflow tailings and
398 a filter sand retrieved from a currently operating tailings dam were tested. The results indicated
399 that the reduction in hydraulic conductivity during compression is significantly amplified if the
400 stresses were sufficiently high to cause grain breakage, mainly due to the increased fines content
401 in the soil matrix. The experimental results suggest that a stress increase from 5 MPa to 40 MPa
402 can cause a reduction in hydraulic conductivity by one order of magnitude for both materials. This
403 reduction in hydraulic conductivity may cause increased saturation and a raised phreatic surface
404 inside the tailings dam, increasing the potential for liquefaction and failure of the structure upon
405 external excitations (e.g. earthquakes).

406 The experimental data are interpreted and analyzed within the framework of continuum breakage
407 mechanics theory. The constitutive model based on this theory is equipped with a novel breakage
408 evolution law which is then combined with six empirical hydraulic conductivity models to predict
409 the co-evolution of stress, strain, gradation and hydraulic conductivity of the tailings materials

subjected to high-stress loading. For the underflow tailings and filter sand tested in this study, the Kozeny-Carman, Terzaghi and Breyer models accurately captured the measured hydraulic conductivities up 40 MPa vertical stress. The Breyer model also performed well at stresses greater than 40 MPa. The Slither and Hazen models significantly underpredicted the measured hydraulic conductivity, whereas the USBR model overpredicted the measured hydraulic conductivity at all stresses for the tested materials. The results of this study provide a starting point for future implementation of the model in coupled hydromechanical finite element analysis and for the simulation of full-scale tailings dams that consider grain breakage and hydraulic conductivity evolution. The proposed framework also may be suitable for extension to other applications including time-dependent deformation (Zhang and Buscarnera, 2017) and environmentally assisted degradation (Zhang and Buscarnera 2018) of tailings materials.

DATA AVAILABILITY STATEMENT

Some or all data, models, or code that support the findings of this study are available from the corresponding author upon reasonable request.

ACKNOWLEDGMENT

Yida Zhang wishes to thank Stantec Inc. for providing the testing materials and the financial support for this study. The startup fund provided by the University of Colorado-Boulder is also gratefully acknowledged. The authors also thank the editor and the anonymous reviewers for their constructive comments which have made great improvements of this paper.

REFERENCES

Alyamani, M. S., and Şen, Z. 1993. "Determination of hydraulic conductivity from complete grain‐size distribution curves." *Groundwater*, 31(4), 551-555.https://doi.org/10.1111/j.1745-6584.1993.tb00587.x

Ashari, S. E., Das, A., and Buscarnera, G. 2016. "Continuum modeling of the effect of surface area growth due to crushing and damage on the permeability of granular rocks." *arXiv preprint*, arXiv:1612.03221

ASTM D854-14, Standard Test Methods for Specific Gravity of Soil Solids by Water Pycnometer, ASTM International, West Conshohocken, PA, 2014, www.astm.org

ASTM D1140-17, Standard Test Methods for Determining the Amount of Material Finer than 75-μm (No. 200) Sieve in Soils by Washing, American Standard of Testing Materials, West Conshohocken, PA, 2017, www.astm.org

ASTM D2487-17e1, Standard Practice for Classification of Soils for Engineering Purposes (Unified Soil Classificiation System), ASTM International, West Conshohocken, PA, 2017,

ASTM D4253-16e1, Standard Test Methods for Maximum Index Density and Unit Weight of Soils Using a Vibratory Table, American Standard of Testing Materials, West Conshohocken, PA, 2016, www.astm.org

ASTM D4254-16, Standard Test Methods for Minimum Index Density and Unit Weight of Soils and Calculation of Relative Density, American Standard of Testing Materials, West Conshohocken, PA, 2016, www.astm.org

ASTM D5856-15, Standard Test Method for Measurement of Hydraulic Conductivity of Porous Material Using a Rigid-Wall, Compaction-Mold Permeameter, ASTM International, West Conshohocken, PA, 2015, www.astm.org

Bardet, J.-P. 1997. *Experimental soil mechanics*, Prentice Hall Upper Saddle River, NJ.

Barrera, S., Valenzuela, L., and Campaña, J. 2011. "Sand tailings dams: design, construction and operation." *Proc., Proceedings of Tailings and Mine Waste*, Vancouver, BC.

Bebbington, A., Hinojosa, L., Bebbington, D. H., Burneo, M. L., and Warnaars, X. 2008. "Contention and ambiguity: Mining and the possibilities of development." *Development and Change*, 39(6), 887-914.https://doi.org/10.1111/j.1467-7660.2008.00517.x

Bedin, J., Schnaid, F., Da Fonseca, A., and Costa Filho, L. D. M. 2012. "Gold tailings liquefaction under critical state soil mechanics." *Géotechnique*, 62(3), 263-267.https://doi.org/10.1680/geot.10.P.037

Boadu, F. K. 2000. "Hydraulic conductivity of soils from grain-size distribution: new models." *Journal of Geotechnical and Geoenvironmental Engineering*, 126(8), 739-746.https://doi.org/10.1061/(ASCE)1090-0241(2000)126:8(739)

Burritt, R. L., and Christ, K. L. 2018. "Water risk in mining: Analysis of the Samarco dam failure." *Journal of Cleaner Production*, 178, 196-205.https://doi.org/10.1016/j.jclepro.2018.01.042

Cabalar, A. F., and Akbulut, N. 2016. "Evaluation of actual and estimated hydraulic conductivity of sands with different gradation and shape." *SpringerPlus*, 5(1), 820.https://doi.org/10.1186/s40064-016-2472-2

Carman, P. C. 1956. *Flow of gases through porous media*, Academic Press Inc. Publishers, New York.

Carrier, W. D. 2003. "Goodbye, Hazen; Hello, Kozeny-Carman." *Journal of Geotechnical and Geoenvironmental Engineering*, 129(11), 1054-1056.https://doi.org/10.1061/(ASCE)1090-0241(2003)129:11(1054)

Chaney, R., and Mulilis, J. P. 1978. "Suggested method for soil specimen remolding by wet-raining." *Geotechnical Testing Journal*, 1(2), 107-108.https://doi.org/10.1520/GTJ10378J

Cheng, C., and Chen, X. 2007. "Evaluation of methods for determination of hydraulic properties in an aquifer–aquitard system hydrologically connected to a river." *Hydrogeology Journal*, 15(4), 669-678.https://doi.org/10.1007/s10040-006-0135-z

Colliat-Dangus, J. L., Desrues, J., and Foray, P. 1988. "Triaxial testing of granular soil under elevated cell pressure." *Advanced Triaxial Testing of Soil and Rock*, ASTM International, West Conshohocken, PA.

Creager, W. P., Justin, J. D. W., and Hinds, J. 1945. "Engineering for dams."

Daouadji, A., and Hicher, P. Y. 2010. "An enhanced constitutive model for crushable granular materials." *International journal for numerical and analytical methods in geomechanics*, 34(6), 555-580

Davies, M., Martin, T., and Lighthall, P. 2000. "Mine tailings dams: when things go wrong." *Tailings Dams, Association of State Dam Safety Oficials, US. Committee on Large Dams, Las Vegas, Nevada*, 261-273

DeJong, J. T., and Christoph, G. G. 2009. "Influence of particle properties and initial specimen state on one-dimensional compression and hydraulic conductivity." *Journal of geotechnical and geoenvironmental engineering*, 135(3), 449-454

Einav, I. 2007. "Breakage mechanics—part I: theory." *Journal of the Mechanics and Physics of Solids*, 55(6), 1274-1297.https://doi.org/10.1016/j.jmps.2006.11.003

Einav, I. 2007. "Breakage mechanics—Part II: Modelling granular materials." *Journal of the Mechanics and Physics of Solids*, 55(6), 1298-1320.https://doi.org/10.1016/j.jmps.2006.11.004

Einav, I., and Puzrin, A. M. 2004. "Pressure-dependent elasticity and energy conservation in elastoplastic models for soils." *Journal of Geotechnical and Geoenvironmental engineering*, 130(1), 81-92.https://doi.org/10.1061/(ASCE)1090-0241(2004)130:1(81)

Fourie, A., and Papageorgiou, G. 2001. "Defining an appropriate steady state line for Merriespruit gold tailings." *Canadian Geotechnical Journal*, 38(4), 695-706.https://doi.org/10.1139/t00-111

Gao, S., Zhang, Y. D., Sonta, A., and Buscarnera, G. 2016. "Evolution of the water retention characteristics of granular materials subjected to grain crushing." *Journal of Geotechnical and Geoenvironmental Engineering*, 142(9), 06016006.https://doi.org/10.1061/(ASCE)GT.1943-5606.0001505

Ghionna, V. N., and Porcino, D. 2006. "Liquefaction resistance of undisturbed and reconstituted samples of a natural coarse sand from undrained cyclic triaxial tests." *Journal of Geotechnical and Geoenvironmental Engineering*, 132(2), 194-202.https://doi.org/10.1061/(ASCE)1090-0241(2006)132:2(194)

Hagerty, M., Hite, D., Ullrich, C., and Hagerty, D. 1993. "One-dimensional high-pressure compression of granular media." *Journal of Geotechnical Engineering*, 119(1), 1-18

Hardin, B. O. 1985. "Crushing of soil particles." *Journal of Geotechnical Engineering*, 111(10), 1177-1192

Hazen, A. 1911. "Discussion: Dams on sand foundations." *Transactions, American Society of Civil Engineers*, 73(11)

Hendron Jr, A. 1963. "The behavior of sand in one-dimensional compression." ILLINOIS UNIV AT URBANA-CHAMPAIGN CHAMPAIGN United States

Ishaku, J., Gadzama, E., and Kaigama, U. 2011. "Evaluation of empirical formulae for the determination of hydraulic conductivity based on grain-size analysis." *Journal of Geology and Mining Research*, 3(4), 105-113.https://doi.org/10.5897/JGMR.9000021

Kozeny, J. 1927. "Uber kapillare leitung der wasser in boden." *Royal Academy of Science, Vienna, Proc. Class I*, 136, 271-306

Mair, K., and Abe, S. 2008. "3D numerical simulations of fault gouge evolution during shear: Grain size reduction and strain localization." *Earth and Planetary Science Letters*, 274(1-2), 72-81.https://doi.org/10.1016/j.epsl.2008.07.010

McDowell, G., Bolton, M., and Robertson, D. 1996. "The fractal crushing of granular materials." *Journal of the Mechanics and Physics of Solids*, 44(12), 2079-2101

McDowell, G. 2002. "On the yielding and plastic compression of sand." *Soils and foundations*, 42(1), 139-145

Milan, V., and Andjelko, S. 1992. *Determination of hydraulic conductivity of porous media from grain-size composition*, Water Resources Publication.

Nakata, Y., Kato, Y., Hyodo, M., HYDE, A. F., and Murata, H. 2001. "One-dimensional compression behaviour of uniformly graded sand related to single particle crushing strength." *Soils and Foundations*, 41(2), 39-51

Nguyen, G. D., and Einav, I. 2009. "The energetics of cataclasis based on breakage mechanics." *Pure and Applied Geophysics*, 166(10-11), 1693-1724.https://doi.org/10.1007/s00024-009-0518-x

Obermeyer, J., and Alexieva, T. 2011. "Design, construction and operation of a large centerline tailings storage facility with high rate of rise." *Proc., Tailings and Mine Waste*, Vancuover, BC.

Odong, J. 2007. "Evaluation of empirical formulae for determination of hydraulic conductivity based on grain-size analysis." *Journal of American Science*, 3(3), 54-60

Park, J. S. 2018. "High Pressure Isotropic Compression and Grain Crushing of Coarse Granular Materials." Master Diss., University of Colorado at Boulder

Pestana, J. M., and Whittle, A. 1995. "Compression model for cohesionless soils." *Géotechnique*, 45(4), 611-632

Riemer, M., Moriwaki, Y., and Obermeyer, J. 2008. "Effect of high confining stresses on static and cyclic strengths of mine tailing materials." *Geotechnical earthquake engineering and soil dynamics IV*, 1-10.

Rogich, D. G., and Matos, G. R. 2008. *Global Flows of Metals and Minerals*, US Department of the interior, US Geological Survey.

Sammis, C., King, G., and Biegel, R. 1987. "The kinematics of gouge deformation." *Pure and Applied Geophysics*, 125(5), 777-812

Slichter, C. S. 1902. "The motions of underground waters." Govt. Print. Off.

Terzaghi, K., and Peck, R. B. 1964. *Soil mechanics in engineering practice*, John Wiley & Sons.

Thompson, F., de Oliveira, B. C., Cordeiro, M. C., Masi, B. P., Rangel, T. P., Paz, P., Freitas, T., Lopes, G., Silva, B. S., and Cabral, A. S. 2020. "Severe impacts of the Brumadinho dam failure (Minas Gerais, Brazil) on the water quality of the Paraopeba River." *Science of The Total Environment*, 705, 135914

Tsoungui, O., Vallet, D., and Charmet, J.-C. 1999. "Numerical model of crushing of grains inside two-dimensional granular materials." *Powder technology*, 105(1), 190-198

Valenzuela, L. 2018. "Design, construction, operation and the effect of fines content and permeability on the seismic performance of tailings sand dams in Chile." *Obras y Proyectos*(19), 6-22.https://doi.org/10.4067/S0718-28132016000100001

Xiao, Y., Liu, H., Ding, X., Chen, Y., Jiang, J., and Zhang, W. 2016. "Influence of particle breakage on critical state line of rockfill material." *International Journal of Geomechanics*, 16(1), 04015031.https://doi.org/10.1061/(ASCE)GM.1943-5622.0000538

Yamamuro, J. A., and Lade, P. V. 1996. "Drained sand behavior in axisymmetric tests at high pressures." *Journal of Geotechnical Engineering*, 122(2), 109-119

Zhang, C., Nguyen, G., and Einav, I. 2013. "The end-bearing capacity of piles penetrating into crushable soils." *Géotechnique*, 63(5), 341

Zhang, Y., and Buscarnera, G. 2017. "A rate-dependent breakage model based on the kinetics of crack growth at the grain scale." *Géotechnique*, 67(11), 953-967

Zhang, Y., and Buscarnera, G. 2018. "Breakage mechanics for granular materials in surface-reactive environments." *Journal of the Mechanics and Physics of Solids*, 112, 89-108.https://doi.org/10.1016/j.jmps.2017.11.008

Zhang, Y., and Buscarnera, G. 2015. "Prediction of breakage-induced couplings in unsaturated granular soils." *Géotechnique*, 65(2), 135-140.https://doi.org/10.1680/geot.14.P.086

Zhang, Y., Park, J., Gao, S., Sonta, A., Horin, B., and Buscarnera, G. 2017. "Effect of grain crushing and grain size on the evolution of water retention curves." *PanAm Unsaturated Soils 2017*, 268-278.

Zhang, Y., Buscarnera, G., and Einav, I. 2016. "Grain size dependence of yielding in granular soils interpreted using fracture mechanics, breakage mechanics and Weibull statistics." *Géotechnique*, 66(2), 149-160.https://doi.org/10.1680/jgeot.15.P.119

Zhou, X., Ma, G., and Zhang, Y. 2019. "Grain size and time effect on the deformation of rockfill dams: a case study on the Shuibuya CFRD." *Géotechnique*, 69(7), 606-619.https://doi.org/10.1680/jgeot.17.P.299

APPENDIX A

The breakage energy E_B for pressure-dependent elasticity can be obtained from Eq. (12) as:

$$E_B = -\frac{\partial \Psi}{\partial B} = -\frac{\partial \left(1-\vartheta B\right)\psi}{\partial B} = \vartheta\left(\frac{p_r}{\bar{K}\left(2-m\right)}A^{\frac{2-m}{1-m}} + \frac{3}{2}p_r\bar{G}A^{\frac{m}{1-m}}\varepsilon_s^{e2}\right) \tag{14}$$

Eq. (14) can be re-written in the terms of stresses by substituting the elastic relations (Nguyen and Einav 2009):

$$E_B = \vartheta\left(\frac{p_r}{\bar{K}\left(2-m\right)}A^{\frac{2-m}{1-m}} + \frac{q^2A^{\frac{-m}{1-m}}}{6p_r\bar{G}\left(1-\vartheta_m B\right)^2}\right) \tag{15}$$

where A is defined as

$$A = \left(\frac{A^*}{1-\vartheta B}\right)^{1-m} \text{ with } A^* = \frac{1}{p_r}\left(\frac{p}{2} + \sqrt{\left(\frac{p}{2}\right)^2 - \frac{m\bar{K}}{6\bar{G}}q^2}\right) \tag{16}$$

The expression of mean stress *p* and deviatoric stress *q* can be obtained from Eq. (12) as:

$$p = \frac{\partial \Psi}{\partial \varepsilon_v^e} = \left(1-\vartheta B\right)p_r\bar{K}\bar{A}^{\frac{1}{1-m}}\left(\frac{1}{\bar{K}} + \frac{3}{2}m\bar{G}\bar{A}^{-2}\varepsilon_s^{e2}\right);\ q = \frac{\partial \Psi}{\partial \varepsilon_s^e} = \left(1-\vartheta B\right)3p_r\bar{G}\bar{A}^{\frac{m}{1-m}}\varepsilon_s^e \tag{17}$$

where $\bar{A} = \bar{K}(1-m)\varepsilon_v^e + 1$. Enforcing consistency condition by combining Eqs. (7), (11), (12) and (17), the expression of λ can be obtained as:

$$\lambda = \frac{\frac{\partial y}{\partial p}\frac{\partial p}{\partial \varepsilon_v^e}d\varepsilon_v + \frac{\partial y}{\partial q}\frac{\partial q}{\partial \varepsilon_s^e}d\varepsilon_s}{\frac{\partial y}{\partial p}\frac{\partial p}{\partial \varepsilon_v^e}\frac{\partial \bar{y}}{\partial \bar{p}} + \frac{\partial y}{\partial q}\frac{\partial q}{\partial \varepsilon_s^e}\frac{\partial \bar{y}}{\partial \bar{q}} - \left(\frac{\partial y}{\partial p}\frac{\partial p}{\partial B} + \frac{\partial y}{\partial q}\frac{\partial q}{\partial B} + \frac{\partial y}{\partial B}\right)\frac{\partial \bar{y}}{\partial E_B}} \tag{18}$$

where

601 $$\frac{\partial y}{\partial p}=\frac{1}{E_c^*}\frac{\partial E_B}{\partial p}-2\left(\frac{q}{M}\right)^2\frac{1}{p^3};\frac{\partial y}{\partial q}=\frac{1}{E_c^*}\frac{\partial E_B}{\partial q}+\frac{2q}{(Mp)^2}$$

602 $$\frac{\partial p}{\partial \varepsilon_v^e}=(1-\vartheta B)\left(p_r A^{\frac{m}{1-m}}\bar{K}+\frac{3}{2}p_r\bar{G}\bar{K}mA^{\frac{3m-2}{1-m}}\bar{K}(2m-1)\varepsilon_s^{e2}\right);\ \frac{\partial q}{\partial \varepsilon_s^e}=(1-\vartheta B)\left(3p_r\bar{G}A^{\frac{m}{1-m}}\right)$$

603 $$\frac{\partial p}{\partial B}=-\vartheta B p_r\bar{K}A^{\frac{1}{1-m}}\left(\frac{1}{\bar{K}}+\frac{3}{2}m\bar{G}A^{-2}\varepsilon_s^{e2}\right);\ \frac{\partial q}{\partial B}=-\vartheta\left(3p_r\bar{G}A^{\frac{m}{1-m}}\varepsilon_s^e\right)$$

604 $$\frac{\partial \overline{y}}{\partial \overline{p}}=\frac{2E_B\sin^2 w}{pE_c^*};\ \frac{\partial \overline{y}}{\partial \overline{q}}=\frac{2q}{(Mp)^2};\ \frac{dy}{dB}=\frac{1}{E_c^*}\frac{\partial E_B}{\partial B}-\left(\frac{E_B}{E_c^{*2}}\right)\frac{\partial E_c^*}{\partial B};\ \frac{\partial \overline{y}}{\partial E_B}=\frac{2\cos^2 w}{E_c^*};\ \frac{\partial E_c^*}{\partial B}=\frac{sE_c}{(1-B)^{s+1}}$$

605 $$\frac{\partial E_B}{\partial B}=\frac{(2-m)\vartheta^2}{(1-\vartheta B)^{3-m}}\left(\frac{p_r}{\bar{K}(2-m)}A^{*\frac{2-m}{1-m}}+\frac{q^2A^{*\frac{-m}{1-m}}}{6p_r\bar{G}}\right)$$

606 $$\frac{\partial E_B}{\partial p}=\frac{\vartheta\left(A^*\right)^{1-m}}{2p_r(1-\vartheta B)^{2-m}}\left[\left(1+\frac{p}{2}\left(\frac{p^2}{4}-\frac{m\bar{K}}{6\bar{G}}q^2\right)^{-\frac{1}{2}}\right)\left(\frac{p_r}{\bar{K}}-\frac{mq^2}{A^{*2}6p_r\bar{G}}\right)\right]$$

607 $$\frac{\partial E_B}{\partial q}=\frac{\vartheta\left(A^*\right)^{1-m}}{6\bar{G}(1-\vartheta B)^{2-m}}\left[-mq\left(\frac{p^2}{4}-\frac{m\bar{K}}{6\bar{G}}q^2\right)^{-\frac{1}{2}}+\frac{q}{A^*p_r}\left(2+\frac{m^2q^2\bar{K}}{6\bar{G}A^*p_r}\left(\frac{p^2}{4}-\frac{m\bar{K}}{6\bar{G}}q^2\right)^{-\frac{1}{2}}\right)\right]$$

608 In numerical integration, the incremental plastic strains and the incremental breakage are
609 calculated using Eqs. (11) and (18). The elastic strains are updated using Eq. (18).

Caption List:

Fig. 1 (a) Initial grain size distribution of underflow tailings and filter sand; Images of uncrushed (b) Underflow tailings (c) Filter sand

Fig. 2. The (a) 3D cross section and (b) picture of the assembled oedometer cell; (c) the combined loading and hydraulic conductivity test setup

Fig. 3. (a) The flow path in the HSP cell and (b) a conceptualized 1D flow system

Fig. 4. Correlation experiments and curves for hydraulic conductivity measured from oedometer vs. hydraulic conductivity measured from permeameter

Fig. 5. Compression curve, hydraulic conductivity, and GSD curves at different stress levels for (a, b) underflow tailings and (c, d) filter sands

Fig. 6. Effect of (a) shape factor with E_c=0.08 MPa and (b) critical breakage energy with s=5 on p-B relation under isotropic compression. Experimental data from Park (2018)

Fig. 7. Model vs. data on compression response, breakage evolution, and GSD evolution of (a, b) underflow tailings and (c, d) filters sand

Fig. 8. Model vs. data on hydraulic conductivity for (a) underflow tailings and (b) filter sand

631 **Table 1:** Basic properties of Materials

	Material Type		Reference
	Underflow	Filter	
Fines Content (%)	19	6	(ASTM D1140-17)
d_{10} (mm)	0.027	0.13	(ASTM D1140-17)
d_{20} (mm)	0.076	0.3	(ASTM D1140-17)
d_{30} (mm)	0.1	0.45	(ASTM D1140-17)
d_{60} (mm)	0.18	1	(ASTM D1140-17)
Coefficient of Uniformity, C_u	16.36	7.69	(ASTM D2487-17e1 2017)
Coefficient of Curvature, C_c	5.05	1.55	(ASTM D2487-17e1 2017)
Unified Soil Classification System	Silty Sand (SM)	Well graded Sand (SW)	(ASTM D2487-17e1 2017)
Specific gravity, G_s	2.73	2.64	(ASTM D854-14)
Maximum void ratio	1.027	0.75	(ASTM D4254-16)
Minimum void ratio	0.48	0.49	(ASTM D4253-16e1)
Maximum dry density (kg/m^3)	1830	1770	(ASTM D4254-16)
Minimum dry density (kg/m^3)	1350	1500	(ASTM D4253-16e1)

* d_{10}, d_{20}, d_{30}, and d_{60} are the grain diameters with 10%, 20%, 30% and 60% cumulative weight of the sample from the GSD curve, respectively. Coefficient of uniformity is given by $C_u=d_{60}/d_{10}$. Coefficient of Curvature is given by $C_c=d_{30}^2/(d_{10} \text{ x } d_{60})$

632

633 **Table 2:** $k_a - k_s$ correlation parameters

Sample Height (mm)	A	B (mm/s)	n
38	4×10^3	1.4×10^{-5}	0.9
25	8×10^3	1.4×10^{-5}	0.7
15	1.2×10^4	1.4×10^{-5}	0.6

634

635

636

637

638

639

640

641

642 **Table 3**: Expressions of the coefficient for various hydraulic conductivity models

Model	Porosity function, $\varphi(n)$	Sorting coefficient, C	Effective grain diameter, d_e (mm)	Reference
Kozeny-Carman	$\frac{n^3}{(1-n)^2}$	8.3×10^{-3}	d_{10}	Carman (1956)
Breyer	1	$6\times10^{-4}\log\frac{500}{C_u}$	d_{10}	Milan and Andjelko (1992)
Slitcher	$n^{3.287}$	1×10^{-2}	d_{10}	Slichter (1902)
Terzaghi	$\left(\frac{n-0.13}{\sqrt[3]{1-n}}\right)^2$	$6.1\times10^{-3} < C < 10.7\times10^{-3}$	d_{10}	Terzaghi and Peck (1964)
Hazen	$1+10(n-0.26)$	6×10^{-4}	d_{10}	Hazen (1911)
USBR	1	$4.8\times10^{-4}d_{20}^{0.3}$	d_{20}	Creager et al. (1945)

* C_u represents the coefficient of uniformity and is given by $C_u=d_{60}/d_{10}$, where d_{60} and d_{10} are the grain diameters with 60% and 10% cumulative weight of the sample from the GSD curve.

643

644 **Table 4**: CBM parameters

Materials	GSD parameters				Mechanical Parameters					
	d_m (mm)	d_M (mm)	β	ϑ	$\bar{K}$	$\bar{G}$	E_c (MPa)	s	ω	M
Tailings Underflow	0.001	0.425	2.0	0.256	1470	1620	0.11	2.5	15	1.5
Filter Sands	0.001	2	2.15	0.510	1960	2125	0.08	2.5	20	1.5

645

Figure

Click here to access/download;Figure;Fig1.pdf

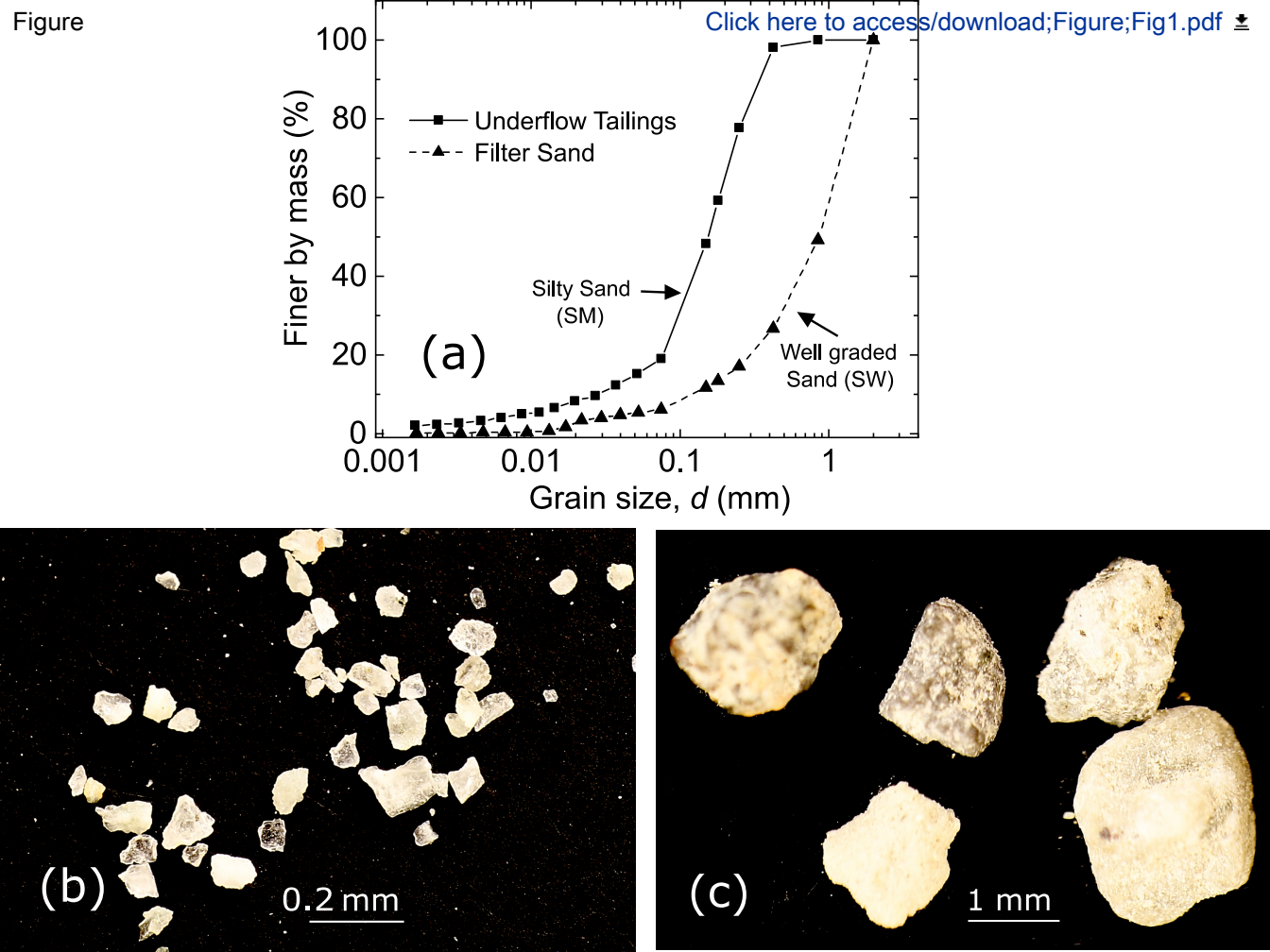

Figure

Click here to access/download;Figure;fig2.pdf

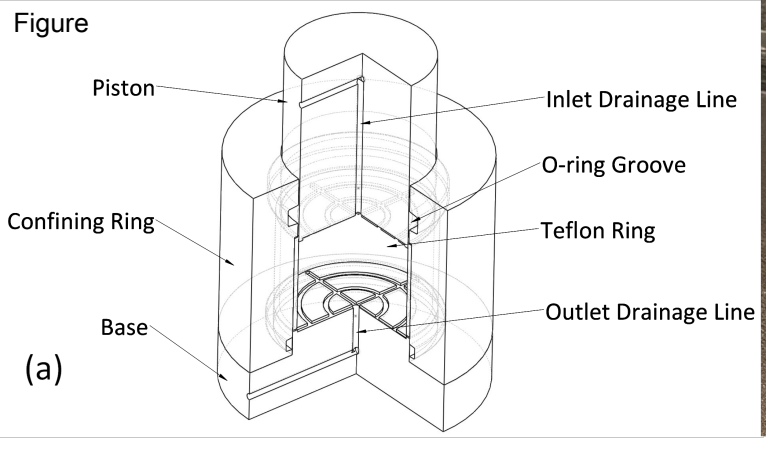

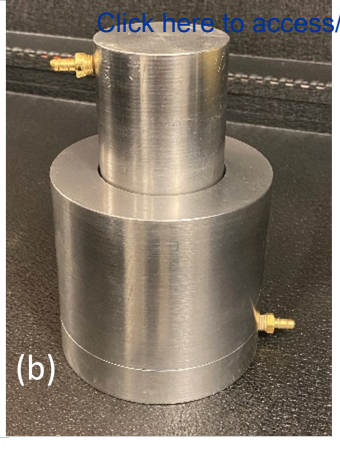

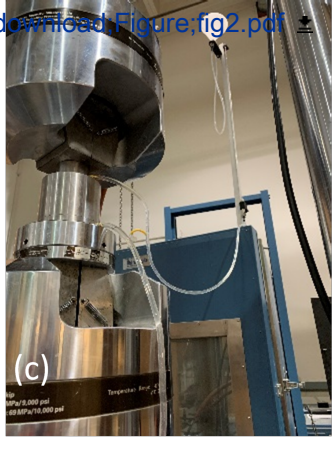

Figure

Click here to access/download;Figure;Fig3.pdf

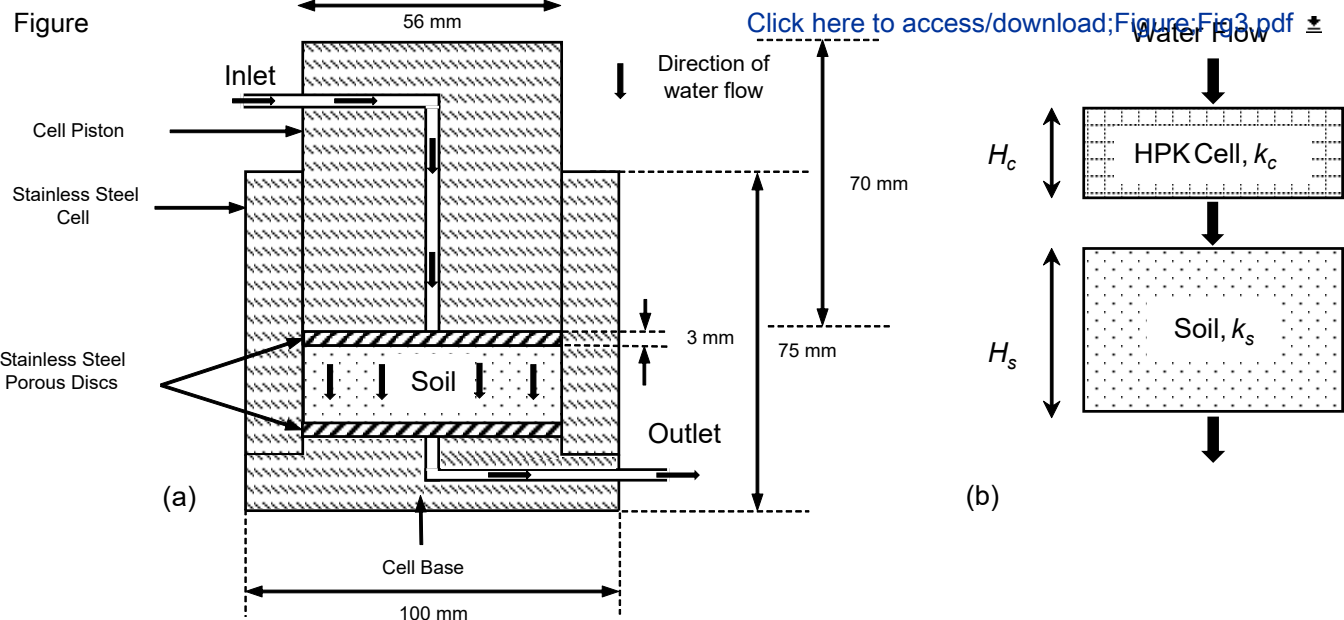

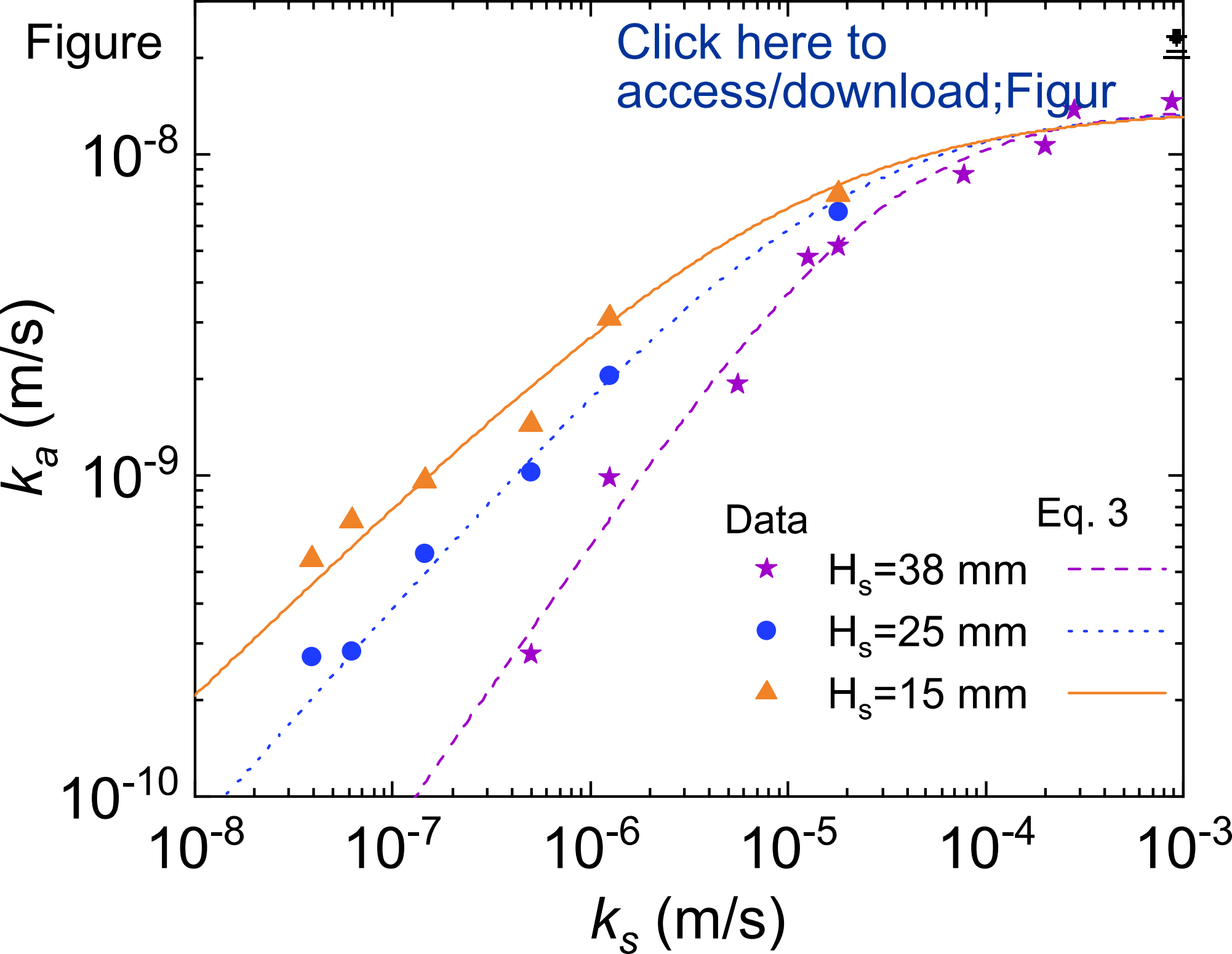
Figure
Click here to access/download;Figur
10^{-8}
10^{-9}
10^{-10}
k_a (m/s)
10^{-8}
10^{-7}
10^{-6}
10^{-5}
10^{-4}
10^{-3}
k_s (m/s)
Data
Eq. 3
H_s=38 mm
H_s=25 mm
H_s=15 mm

Figure

Click here to access/download;Figure;Fig5.pdf

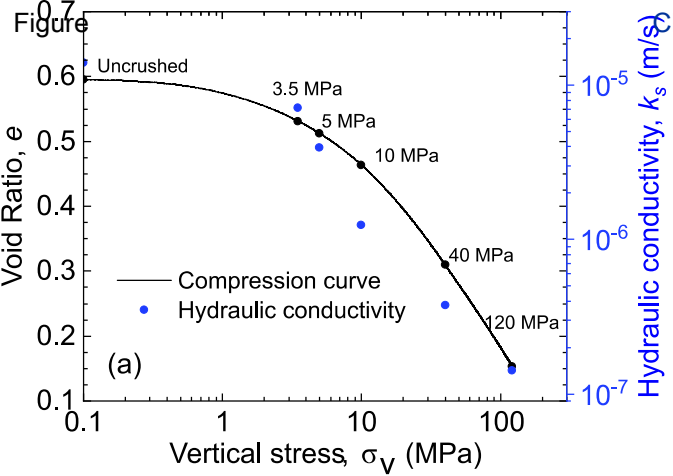

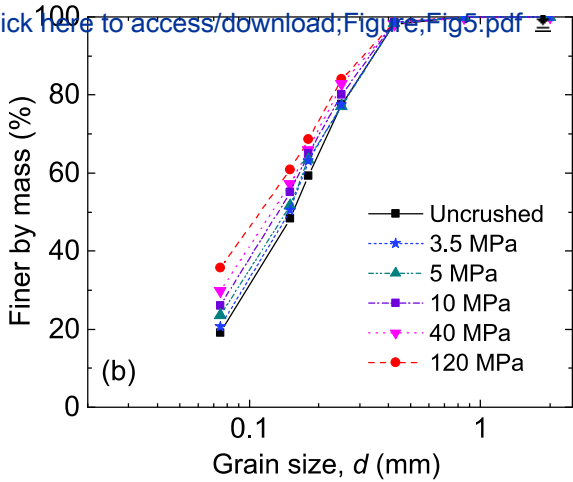

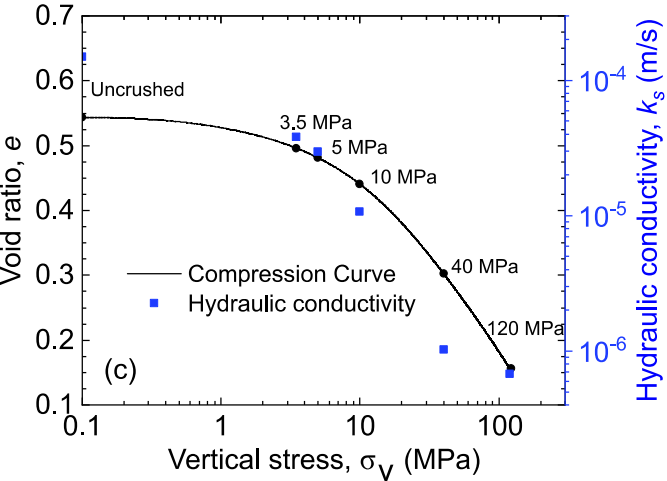

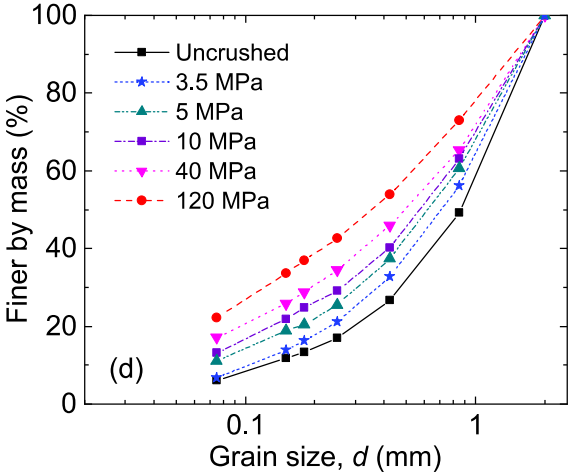

Figure
Click here to access/download;Figure;Fig6.pdf

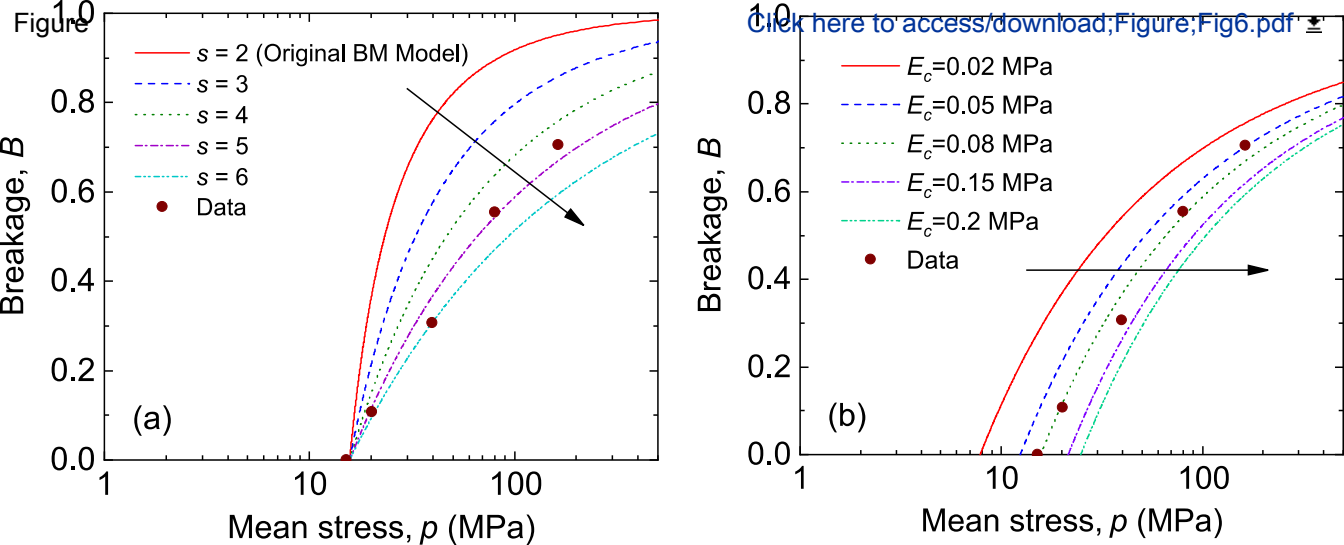

Figure
Click here to access/download;Figure;Fig7.pdf

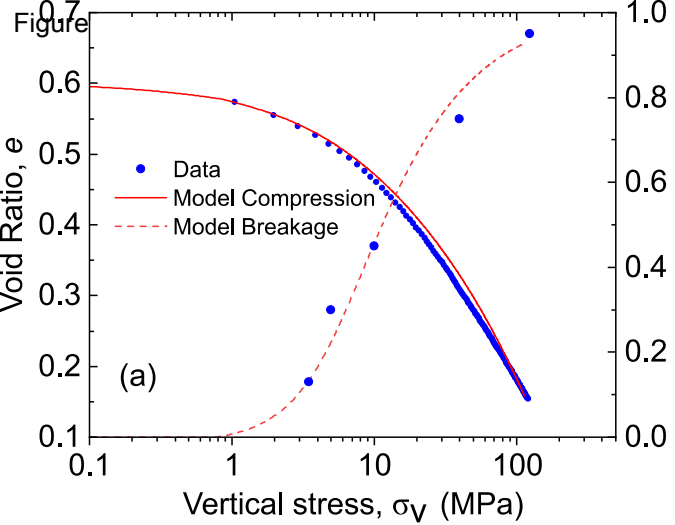

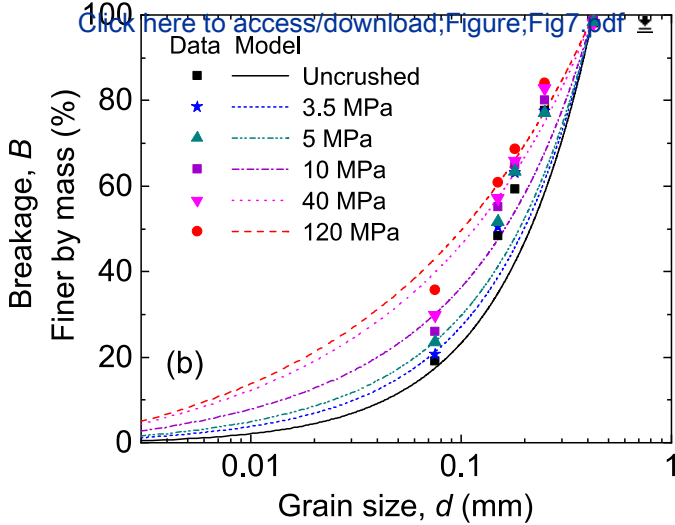

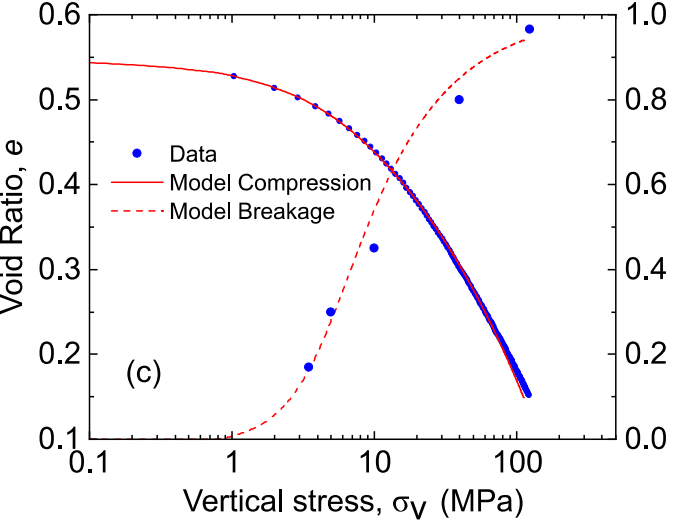

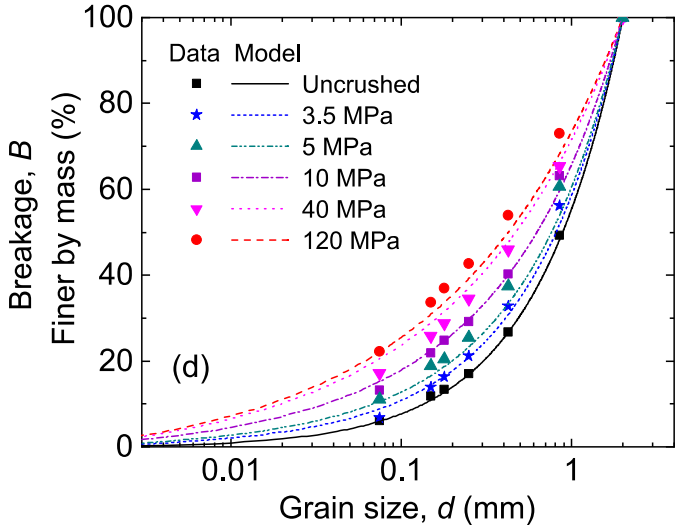

Figure
Click here to access/download;Figur

